ACCSCIENCE PUBLISHING

Materials Science in Additive Manufacturing

ORIGINAL RESEARCH ARTICLE

Technology overview and investigation of the quality of a 3D-printed maraging steel demonstration part

César M. A. Vasques[1,2]*, Adélio M. S. Cavadas[1], and João C. C. Abrantes[1]

[1]proMetheus, Higher School of Technology and Management, Polytechnic Institute of Viana do Castelo (IPVC), Rua Escola Industrial e Comercial de Nun' Álvares, 4900-347, Viana do Castelo, Portugal

[2]Center for Mechanical Technology and Automation (TEMA), Department of Mechanical Engineering, University of Aveiro, Campus Universitário de Santiago, 3810-193 Aveiro, Portugal

Abstract

Additive manufacturing (AM) has gained significant traction in the production of high-performance metallic components, yet concerns persist regarding the consistency of powder materials and the mechanical properties of 3D-printed parts. This study addresses these challenges through a detailed analysis of a maraging steel part manufactured using laser powder bed fusion. The demonstration part was evaluated for geometric accuracy, surface roughness, chemical composition, microstructure, and mechanical properties, including hardness and density. The findings revealed that 3D-printed maraging steel components can achieve high levels of dimensional precision and mechanical integrity, making them suitable for demanding applications. Despite these promising results, the study highlighted the need for improved powder quality control and accurate composition measurement to ensure the consistent production of reliable parts. The non-destructive hardness testing method applied in this study proved effective for predicting tensile strength, offering a streamlined approach to quality assurance. These results contribute to a growing body of research and knowledge supporting the adoption of AM for producing critical mechanical components, while underscoring the need for further investigation into quality assurance and standardized non-destructive testing procedures for high-performance metal AM parts.

Keywords: 3D printing; Additive manufacturing; Laser powder bed fusion; Steel 1.2709; Maraging steel; Quality analysis; Mechanical properties

***Corresponding author:**
César M. A. Vasques
(cmavasques@ua.pt)

Citation: Vasques CMA, Cavadas AMS, Abrantes JCC. Technology overview and investigation of the quality of a 3D-printed maraging steel demonstration part. *Mater Sci Add Manuf.* 2025;4(2):025040002. doi: 10.36922/MSAM025040002

Received: January 21, 2025

Revised: March 3, 2025

Accepted: March 6, 2025

Published online: April 8, 2025

1. Introduction

Additive manufacturing (AM), particularly through laser powder bed fusion (LPBF), commonly also referred to as selective laser melting (SLM), has become a transformative force in modern manufacturing. This technology allows for the creation of customized, high-performance mechanical components with intricate and complex geometries. Unlike traditional subtractive methods such as turning or milling, where material is removed to shape a part, AM builds components layer by layer. This unique process is guided by a 3D model, and with the advent of "design for additive manufacturing", engineers now design parts with both the capabilities and constraints of AM in mind.[1]

The appeal of AM lies in its nearly limitless design possibilities, enabling the fabrication of parts with functionalities that are often unattainable through conventional manufacturing methods. Entire assemblies can be constructed at one go, reducing the need for multiple components and simplifying supply chains. AM constructs components with precision, using only the material required for each layer, making it an ideal solution for creating customized, unique products – even in high-volume production environments. The lack of tooling further streamlines workflows, minimizing setup times and wear, while lightweight designs can be achieved due to the high structural integrity and reduced weight of AM parts. These advantages make AM an attractive option across various industries, offering unprecedented innovation potential and efficiency.[2]

However, despite its tremendous advantages, the path to fully realizing the potential of AM, particularly in metal manufacturing, is fraught with challenges. While laser-based methods, such as LPBF and laser-directed energy deposition, have achieved industrial maturity over the past two decades, several uncertainties and limitations persist. Chief among these concerns is the consistency of feedstock material quality and the mechanical properties of the printed parts, both of which play critical roles in determining the reliability and performance of the final components. Variations in powder quality can lead to inconsistencies in microstructure and mechanical performance, thus affecting the overall reliability of AM-produced parts.[3]

Another major challenge involves testing methodologies and evaluation strategies. In many cases, existing techniques must be refined or completely redesigned to suit the unique characteristics of AM parts. This can be particularly problematic for less experienced users, who may find that traditional designs are incompatible with AM processes. As a result, significant design adaptations are often required to fully exploit AM's capabilities, with multiple iterative tests and validation steps needed to ensure component quality. Addressing these uncertainties is critical to ensuring the long-term success and reliability of metal AM in industrial applications, particularly for high-stakes sectors such as aerospace, automotive, and medical devices.[4]

In recent years, research and development in AM, particularly in the realm of metal 3D printing, have accelerated rapidly. There have been substantial efforts to standardize metal AM techniques and terminology, such as those outlined in International Organization for Standardization (ISO)/American Society for Testing and Materials (ASTM) 52900:2021.[5] However, practical usage in commercial and industrial settings often deviates from these standards. This has led to a variety of similar designations.[6-11] Although the designations vary, the underlying AM processes follow a broadly similar workflow. The process begins with a 3D computer-aided design (CAD) model, which can be developed from scratch, reverse-engineered, or generated through imaging. This model is then sliced into thin layers, each with a thickness ranging from 20 to several hundred microns, depending on the specific AM technique. The part is constructed by depositing material layer by layer and selectively melting it using a heat source, such as a laser or electron beam. Despite the general similarity in process, significant differences exist between methods such as laser beam melting (LBM), electron beam melting, and laser metal deposition, particularly regarding their material deposition strategies, precision, speed, and associated mechanical properties. Understanding these differences is essential for optimizing the production process and ensuring high-quality outcomes, and a thorough discussion on metal AM can be found in the literature.[12]

The quality of AM-produced components is influenced by numerous factors, including powder characteristics, laser energy input, scan speed, and environmental conditions during the build.[13] For instance, the particle size and distribution of the powder directly affect the mechanical properties, surface roughness, and dimensional accuracy of the printed parts.[14-17] One of the most significant challenges is achieving acceptable surface roughness. Due to the nature of the layer-by-layer manufacturing process, LPBF parts typically exhibit high surface roughness values, often exceeding the requirements for high-precision applications. The surface roughness of LPBF parts is influenced by factors such as laser power, scanning strategy, part orientation, and inert gas flow direction.[18] Typically, LPBF parts exhibit arithmetic mean roughness (Ra) values ranging from 5 to 50 μm, depending on the specific process parameters and materials used. Without post-processing, LPBF parts cannot meet strict surface roughness standards, such as Ra below 0.8 μm for machine components or below 1 μm for dental implants. Achieving the desired surface finish often necessitates post-processing methods such as traditional CNC machining.

The LPBF process is highly sensitive to various parameters, such as laser power, scan speed, and powder material properties such as size and morphology. Improper control of these parameters can lead to defects, such as unmolten powder particles, porosity, and cracks, which compromise the mechanical integrity of the final part.[19,20] These defects are typically categorized into three main types: porosities, incomplete fusion holes, and cracks, each requiring careful management through process optimization. Increasing energy density generally helps reduce defects such as balling, thereby improving surface quality, and reducing roughness.

The microstructural characteristics of LPBF components play a crucial role in determining their performance. AM steel grades, which typically exhibit martensitic microstructures in conventional processing, may contain small amounts of retained austenite due to the rapid cooling rates associated with AM.[21] This behavior has been observed in various steels, including precipitation hardening steels like 17-4 PH,[21-23] maraging steels such as 18-Ni300,[24,25] and martensitic stainless steels like AISI420.[26] These rapid cooling rates often lead to fine-grained microstructures, significantly influencing the mechanical properties of the final component.[24,25] Furthermore, the cooling rate, laser parameters, and melt pool size significantly affect the microstructure and texture of AM components, often leading to anisotropy and specific grain orientations that depend on the process parameters.[27-29] It has been demonstrated that components fabricated from AM steel grades frequently exhibit a fine-grained microstructure due to these rapid cooling rates.[12] The boundaries of melt pools can be visible as a superstructure,[28,29] and elongated, oriented grains are commonly observed, depending on the processing parameters.[22,30,31]

The mechanical properties of AM-fabricated steel grades frequently meet or exceed conventional standards for technical applications. Grain refinement leads to significant improvements in yield and ultimate tensile strength. For instance, a low remaining porosity (0.1%) results in ductile failure modes with elongation values comparable to wrought metal.[12] However, a high porosity (2.4%) leads to brittle failure modes and drastically reduced elongation.[32] As such, the static strength of AM components is highly dependent on both the density and microstructure produced during the AM process. AM parts often have finer microstructures than conventionally manufactured components, resulting in higher static strength. The yield strength of AM specimens generally follows the Hall–Petch relationship, as demonstrated in various AM methods, using Ti-6Al-4V.[33] The microstructure of AM-fabricated parts is also anisotropic with respect to the building direction, influencing tensile properties and elongation.[27,34,35] Typically, strength and strain to failure are lower along the build direction than orthogonal to it.

Due to the subtle differences between each AM technique and the hundreds of systems currently available, keeping up with this rapidly evolving technology is challenging. New entrants and quickly developing innovations further complicate purchasing decisions, making it difficult for standards to keep pace. As the metal AM sector progresses toward industrial-scale production, the need for comprehensive global standards has become increasingly critical. Since 2011, the ISO TC/261 and ASTM F42 committees have collaborated to establish unified AM standards, with over 30 joint ISO/ASTM groups working to avoid duplication and streamline resources. In 2016, America Makes and American National Standards Institute launched the Additive Manufacturing Standardization Collaborative to accelerate the creation of industry-wide standards, identifying 93 gaps, including 18 high-priority areas requiring further research. Despite the challenges, collaboration between ISO, CEN, and ASTM ensures the global adoption of these standards, with CEN integrating them into European norms, and regular stakeholder meetings helping to accelerate AM standardization.

Specifically addressing LPBF, recent advancements have enabled the production of complex geometries with high precision. Studies on maraging steels,[36-38] particularly 1.2709, have demonstrated superior mechanical properties, including enhanced strength and toughness when processed through LPBF.[39,40] Furthermore, recent studies have provided new insights into process optimization and microstructural control in LPBF maraging steel,[41,42] reinforcing the relevance of our integrated approach. Although maraging steel fabricated by LPBF has been studied, few works have systematically linked feedstock uniformity, microstructure, and non-destructive mechanical evaluation in a single integrated approach. This gap complicates consistent quality assurance and impedes broader industrial adoption for high-performance applications. Therefore, the present study investigates a 3D-printed maraging steel demonstration part with the following objectives: (1) To characterize powder feedstock morphology and composition to assess uniformity, (2) to analyze the resulting geometry, surface roughness, density, and microstructure of the LPBF-built part, (3) to evaluate mechanical behavior through non-destructive hardness-based methods, and (4) to benchmark our results against established data from the feedstock supplier and existing maraging steel literature. By correlating these findings, we demonstrate a streamlined path for quality assessment in metal AM, bridging feedstock considerations and final part performance. Our integrated analysis thus reinforces the potential of LPBF maraging steel to meet critical mechanical demands, contributing new insights into standardized evaluation procedures for advanced AM applications.

2. Integrated AM: Process, materials, and part fabrication

2.1. LPBF of metals and 3D-printing workflow

Often referred to by different names, powder bed fusion (or melting) is an AM process where thermal energy is

used to selectively fuse specific regions of a powder bed. This method is currently the most widely used for metal 3D printing. In these systems, a thin layer of metal powder is spread across a build platform, and a cross-sectional portion of the part is selectively melted within the powder layer. For clarity, this study will refer exclusively to the LPBF process, in accordance with ISO/ASTM 52900:2021,[5] despite the fact that alternate terminologies such as SLM, LBM, and direct metal laser sintering have also been used in the literature. When strictly adhering to the IST/ASTM standard, the acronym PBF-LB/M specifically applies to laser-based powder bed fusion of metals. Most powder bed fusion systems utilize LPBF technology, where high-powered lasers are used to fuse metal layers together. After printing, an operator extracts the part(s) from the powder bed, detaches them from the build plate, and carries out post-processing. LPBF has become the industry standard for metal AM, with the majority of companies in the field now offering LPBF machines.

As the most mature form of metal 3D printing, LPBF is frequently used as the benchmark against which other technologies are measured. LPBF-printed parts are ideal for precise, geometrically complex components that would be impossible to machine in any other way. They are used in a wide variety of applications, ranging from dentistry to aerospace. Build volumes range from very small (100 mm^3 cube) to very large (800 × 500 × 400 mm^3), with a moderate print speed. Precision is determined by the laser beam width and layer height of these machines. The majority of materials currently available for 3D printing can be used on an LPBF machine.

While these machines are revolutionary, they are limited to industrial users due to a variety of facility and post-processing requirements. LPBF machines must be operated by trained professionals. Due to the intricate nature of the process, numerous components must be printed and tweaked several times before results are obtained. Following printing, the majority of parts require extensive post-processing and heat treatment. In addition, the metal powder that these machines utilize is extremely dangerous and costly to handle; the majority of fully baked LPBF machines cost upwards of $1 million to implement and require a dedicated technician to operate.

In this study, we employed a TRUMPF TruPrint 1000 LPBF system (TRUMPF, Germany) (Figure 1). The machine has a cylindrical build volume of 100 mm in diameter and 100 mm in height, with a 100 W fiber laser and a beam spot diameter of about 55 µm. It operates under an inert argon atmosphere, and layer thicknesses can range from 20 to 50 µm. These features make it suitable for processing maraging steel and other metal powders. The TruPrint

Figure 1. TRUMPF TruPrint 1000 machine, advocated the most productive machine in its class, providing all of the benefits of AM and laser metal fusion for complex, metallic components (top-left); printing in progress of the demonstration tool steel part (top-right); the operating principle of metal 3D printing explained in brief (bottom)
Source: TRUMPF (top left and bottom images)

1000 is capable of producing components in virtually any geometric shape. Even relatively complex shapes can be converted from the CAD design to a 3D metallic component quickly and easily and with excellent quality. The TruPrint 1000 can be used to generate small industrial single parts and series. In addition, you can achieve an increase in productivity of up to 80% and maximum flexibility when processing customer orders with the multilaser option. The multiplate option extends the machine's runtime for the TruPrint 1000. It has a build cylinder that can accommodate up to four substrate plates that change automatically without interrupting the laser metal fusion process. TRUMPF is now advocated to offer the most productive 3D printer system for the dental sector, the TruPrint 1000, for the creation of dental prostheses. In addition, the digital connection to milling stations is a highlight. This enables the development of novel, highly precise dental products. Truprint 1000 is capable of processing a variety of materials, including metal powders for welding, such as stainless steels, tool steels, aluminum, nickel-based alloys (maraging steel), cobalt-chrome, copper, titanium, and precious metal alloys, as well as amorphous metals. On request, the company provides the current availability of materials and their parameters. Aluminum and titanium are only available with the addition of a glove box and a high-resolution oxygen sensor.

The AM process chain begins with the preparation of data for the 3D design and production program. Materialze's intuitive process chain, when combined with the TRUMPF

Build Processor, ensures a high level of process reliability, with tools for development, simulation, 3D printing, and numerical control programming for metal parts that are not integrated into a single system. Converting geometry to STL is required first, and the software package includes a TRUMPF Build Processor that handles slicing and hatching build jobs, as well as parameter management (Figure 2). This well-defined digital printing workflow is efficient, allowing for time and cost savings.

2.2. Maraging steel properties and metallurgy

Steel is a widely utilized engineering material, with numerous alloys that are well-suited for AM due to their excellent weldability and castability. Steel alloys are generally classified into four main groups: carbon steels, alloy steels, stainless steels, and tool steels. Maraging steels, a subset of high-alloy steels, primarily contain 15 – 25% nickel and have a low carbon content. Their strength is derived from the formation of a soft martensitic structure, which undergoes significant hardening through the precipitation of intermetallic compounds during the aging process. Maraging steels offer several advantages that make them particularly appealing for AM. Their exceptional strength-to-weight ratio, outstanding ductility, and excellent fatigue resistance enable the production of lightweight, high-performance components. In addition, their low thermal expansion coefficient and superior thermal stability minimize distortion during the AM process, leading to more precise dimensional accuracy. Although maraging steels are not classified as traditional tool steels, their exceptional malleability, and thermal stability make them suitable for similar applications. As a result, they are sometimes informally referred to as "tool steels."

Various commercial and standardized designations exist for maraging steel powder feedstock similar to that used in this study. Examples include M300 Tool Steel (LPW), Maraging Steel (3D Systems), 1.2709 (EN 10027-2; SLM Solutions; SANDVIK), MS1 (EOS), CL 50WS (Concept Laser), X3NiCoMoTi 18-9-5 (DIN EN 10027-1), Tool Steel 1.2709-A LMF (TRUMPF) and 18Ni-300 (MIL-S-46850D). This kind of steel is characterized by having very good mechanical properties and being easily heat-treatable using a simple thermal age-hardening process. Maraging steels are a subclass of high-strength steels that differ from conventional steels in that they are hardened through a non-carbon metallurgical reaction. Rather than that, these steels are strengthened through the precipitation of intermetallic compounds at temperatures of approximately 500°C. The term "maraging" is derived from martensite age hardening and refers to the age-hardening of a martensite matrix composed of low carbon, iron-nickel laths. Commercial maraging steels are designed to have a yield strength ranging from 1000 to 2400 MPa and certain experimental maraging steels exhibit yield strengths up to nearly 3500 MPa.[43,44] These steels typically contain extremely high amounts of nickel, cobalt, and molybdenum and very little carbon. Indeed, carbon is an impurity in these steels and is kept to a minimum commercially feasible level to avoid the formation of titanium carbide (TiC), which can have a detrimental effect on strength, ductility, and toughness.

Various maraging steel varieties have been developed for specialized applications. Maraging steels are manufactured commercially in the United States and abroad by a variety of steel companies. Due to the absence of carbon and the use of intermetallic precipitation to achieve hardening, maraging steels exhibit several unique properties that distinguish them from conventional steels. Hardenability

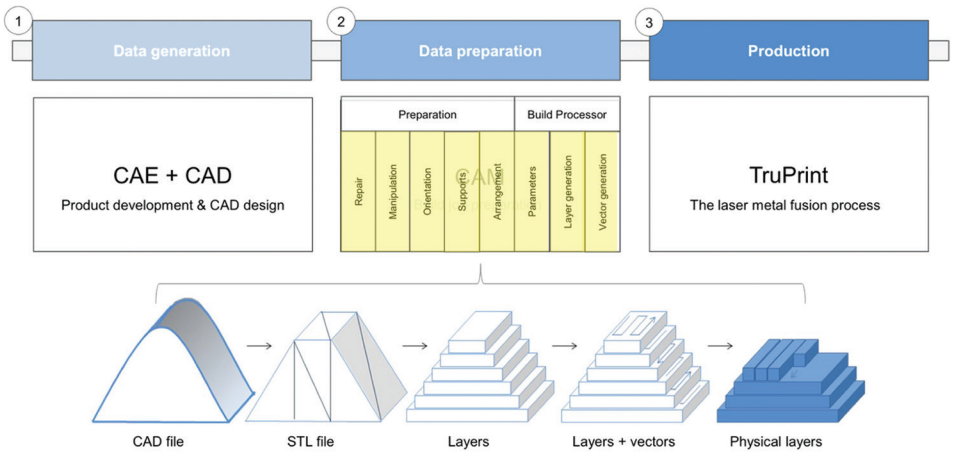

Figure 2. 3D printing digital processing workflow and data preparation for laser metal fusion
Source: TRUMPF

is irrelevant. After annealing, the low-carbon martensite formed is relatively soft (about 35 HRC). There are only very slight dimensional changes during age-hardening. As a result, relatively complex shapes can be machined or 3D-printed in the soft state and then hardened with minimal distortion. This material has excellent weldability and its fracture toughness is significantly higher than that of conventional high-strength steels. This property in particular has resulted in the widespread use of maraging steels in a variety of demanding applications.[45,46]

The 1.2709 maraging steel is a pre-alloyed, ultra-high-strength steel available in powder form. Its composition aligns with the U.S. classification 18% Ni Maraging 300, the European designation 1.2709, and the German standard X3NiCoMoTi 18-9-5. Maraging steels are known for their exceptional strength-to-toughness ratio while maintaining ductility, weldability, and dimensional stability throughout the aging process. Most maraging steel grades exhibit martensite start temperatures between 200°C and 300°C, achieving a fully martensitic structure at room temperature. Consequently, retained austenite is typically not a concern in these alloys, eliminating the need for refrigeration treatments before aging. The resulting martensite is a low-carbon, body-centered cubic (BCC) lath structure characterized by a high dislocation density and the absence of twinning. In its as-built and untreated state, 1.2709 maraging steel exhibits a yield strength (YS) and tensile strength (TS) of approximately 1000 ± 100 MPa and 1100 ± 100 MPa, respectively, with an elongation of 8 ± 3% and a hardness of 33–37 HRC. After aging treatment, these properties improve significantly, reaching 1900 ± 100 MPa for YS, 1950 ± 100 MPa for TS, 2 ± 1% elongation, and a hardness of 50–54 HRC (cf.[47]). These enhanced mechanical characteristics make maraging steel a highly suitable material for AM applications, including automotive components such as gears, drive shafts, springs, and heavy-duty transmissions; aerospace applications such as rocket and missile skins; sports equipment such as fencing blades, bicycle frames, and golf club heads; as well as machinery and tooling across various industries. The readers are referred to a few publications[43,45,46,48] for further technical insight into maraging steels technology.

2.3. 3D-printed part and material sample

The 3D-printed component examined in this study, depicted in Figure 3, is a demonstration piece fabricated using maraging steel feedstock powder, specifically the Tool Steel 1.2709-A LMF grade supplied by TRUMPF. The hollow part contains several intricate geometrical features designed to test the limits of AM capabilities. Its overall projected dimensions fit within a rectangle measuring 69 × 70 mm and a circle with diameter of 90 mm, with a total

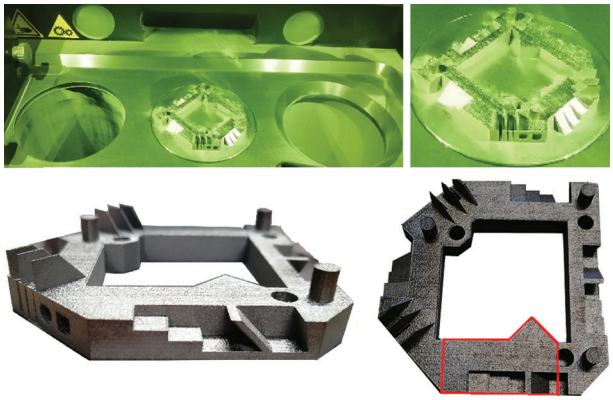

Figure 3. 3D-printed studied maraging steel part as built inside in the machine and connected to the substrate plate (top); final part and cut material sample (bottom)

height of 14 mm. Thin fins and cylinders, each 6 mm in height, are extruded above an 8 mm base plane. The part was 3D-printed using a Truprint 1000 machine with a layer thickness of 20 µm, a laser scanning speed of 600 mm/s, power of 100 W and beam diameter of 55 µm, which were optimized for maraging steel, with a printing time of around 6 hours. As illustrated in Figure 3 (top images), the part was printed within the central cylinder and remained fused to the steel substrate plate upon completion. A Struers Accutom-2 precision cutting machine, equipped with a diamond cut-off wheel, was used to separate the part from the substrate plate and extract a material sample (indicated by the red line in the bottom image) for detailed quality analysis and inspection.

3. Part characterization and quality analysis

3.1. Feedstock powder material characterization

The feedstock powder used for fabricating the demonstration part, designated as Tool Steel 1.2709-A LMF, was supplied by TRUMPF. To ensure powder quality, analyses of particle size distribution, morphology, and chemical composition were conducted. The morphology and chemical composition were examined using a Hitachi SU1510EM Scanning Electron Microscope (SEM) (Hitachi, Japan), while particle size distribution was assessed with a Malvern MS3000 laser diffraction analyzer (Malvern Instruments, United Kingdom), providing fast, accurate, and reliable measurements. Figure 4 presents the particle morphology, revealing predominantly spherical particles with minimal agglomeration and surface irregularities, indicative of high-quality powder with a low risk of defects. A high-magnification (3000×) image of a particle surface is also displayed in Figure 5. Chemical composition analysis was performed using an SEM equipped with a Bruker Quantax 200 detector for Energy-Dispersive X-ray Spectroscopy (Bruker Corporation, United States).

The results exhibited slight variations when compared to typical values provided by material suppliers, as detailed in Table 1.

Although the measured Ni content (14.39 wt.%) fell below the nominal range (17 – 19 wt.%), subsequent analysis confirmed that this shortfall did not significantly impact the printing process, mechanical properties, or phase stability of the maraging steel. In these alloys, Ni is crucial for stabilizing the martensitic phase and promoting intermetallic precipitation during aging,[25] and small Ni fluctuations can shift the martensitic start and finish temperatures, potentially altering the fraction of retained austenite.[45] Nevertheless, our hardness and mechanical tests revealed that the modest Ni deviation did not measurably affect the martensitic matrix or precipitation hardening response. Further investigation into the powder production process is necessary to fully elucidate the origin of this discrepancy.

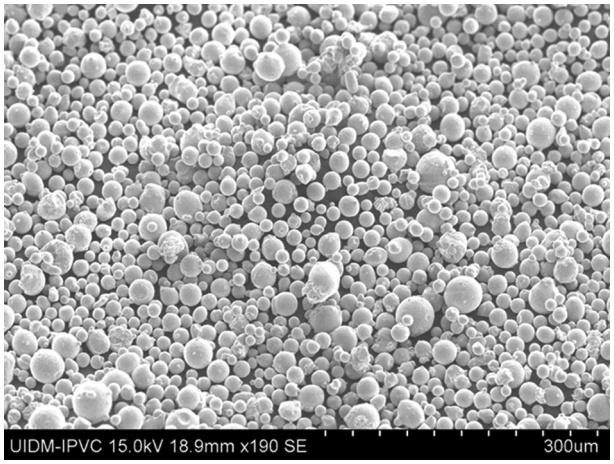

Figure 4. Scanning electron microscopy image at 190× magnification of Tool Steel 1.2709-A LMF (TRUMPF) powder particles
Abbreviation: SEM: Scanning electron microscopy

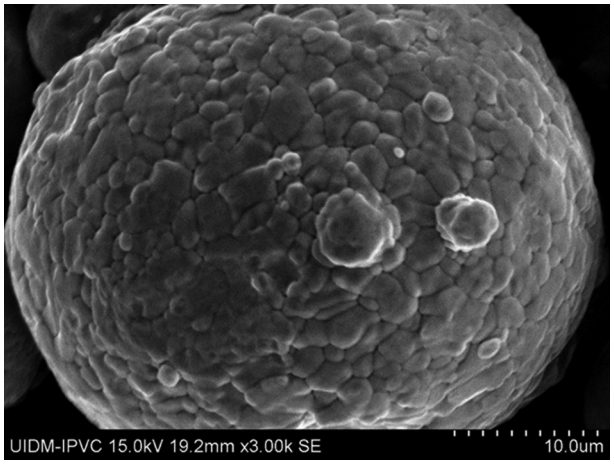

Figure 5. Scanning electron microscopy image at 3000× magnification of Tool Steel 1.2709-A LMF (TRUMPF) powder particle
Abbreviation: SEM: Scanning electron microscopy

As anticipated, the particle size distribution shown in Figure 6 exhibits a Gaussian-like trend, with characteristic values of d_{10} = 17.5, d_{50} = 29.8, and d_{90} = 50.7 µm. However, these values are slightly lower than those typically reported by commercial suppliers, whose size range falls between 20 and 60 µm.[49] Furthermore, Figure 4 reveals a notable presence of satellite particles with diameters around 15 µm. It is important to note that powder particles smaller than 10–20 µm can negatively impact powder flowability and should generally be minimized. However, no flow-related issues were encountered during the manufacturing process. The powder spread evenly and smoothly across the build platform, forming a uniform layer free of air voids. This behavior can be attributed to the high surface quality and consistent particle morphology of the powder, both of which are essential for optimal flowability.[50] As a result, no significant surface defects, such as porosity, were detected in the final printed part, allowing for reduced surface roughness. To ensure measurement consistency, multiple tests were conducted to minimize the relative standard deviation, as shown in Figure 6, where five analyses were performed for each of the eight tests presented.

3.2. Visual inspection, dimensional quality, and roughness

The maraging steel demonstration part shown in Figure 3 was 3D-printed in approximately six hours without requiring any support structures. It was produced directly from the WZA file generated by the TRUMPF Build Processor, in the lay-down orientation illustrated. The final part exhibits excellent visual quality, dimensional accuracy, and repeatability, even for intricate features such as thin shark fins, inclined planes, extrusions, and both cylindrical and squared-shaped holes.

This section also presents the results of a two-dimensional (2D) surface roughness analysis, where Ra was the primary measured parameter (Figures 7 and 8). Two different roughness measurement instruments were

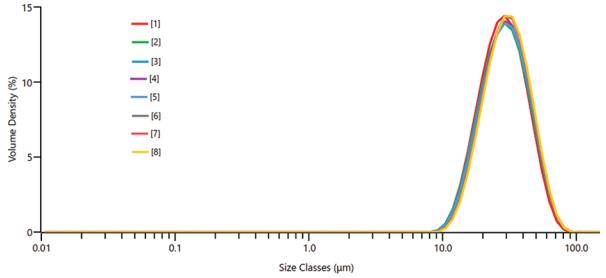

Figure 6. Particle size distribution of Tool Steel 1.2709-A LMF (TRUMPF) powder. Five analyses were run for each of the eight tests shown

Table 1. Typical chemical composition of the Tool Steel 1.2709-A LMF (TRUMPF) powder (wt%) and SEM-measured values. [38,47]

	Ni	Co	Mo	Ti	Cr	Al	Si, Mn	S, P	C	Fe
Nominal	17–19	8.5–11	4.5–6	0.6–1.2	<0.5	0.05–0.15	<0.1	<0.01	<0.02	balance
Measured	14.39	10.73	4	1.36	–	–	–	–	–	Balance

Abbreviation: SEM: Scanning electron microscopy.

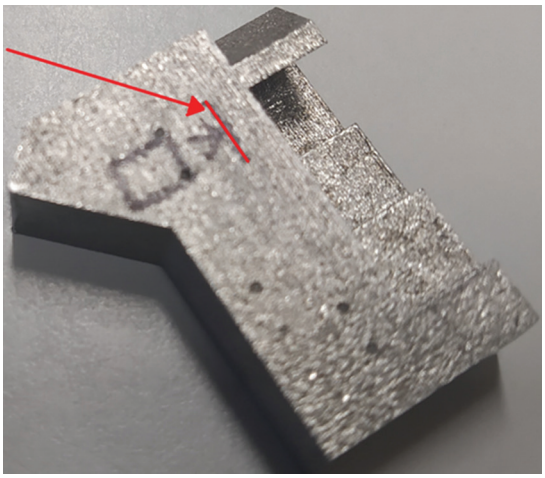

Figure 7. Material sample and roughness measurement line

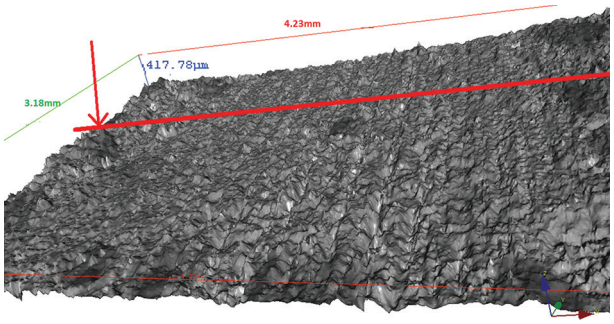

Figure 8. Roughness surface measured with scanning electron microscopy

utilized: the Mitutoyo SJ-210 roughness tester and a SEM. The investigation focused on two distinct surface types. The advancement of 3D printing technology has enabled metallic components produced through the LPBF method to achieve superior mechanical properties compared to those manufactured through conventional techniques.[51,52] However, a well-documented drawback of 3D-printed parts – particularly those fabricated using LPBF – is their inherently high surface roughness due to the nature of the AM process, as examined previously.[53-56] While various roughness parameters exist, Ra, which represents the arithmetic mean deviation of the filtered roughness profile from the central line over a given evaluation length, is the most commonly used metric. This predominance is largely historical, stemming from the limitations of early roughness meters, which could only measure Ra, rather than from any inherent technical superiority. The arithmetical mean deviation of the assessed profile on LPBF-produced 3D-printed parts typically ranges from 5 to 50 µm, though it is generally found to be below 20 µm, as reported previously.[54]

3.3. Density testing

The density of the maraging steel was determined using the buoyancy method, which is based on Archimedes' principle and conducted in distilled water. According to this principle, an object submerged either partially or fully in a fluid experiences an upward buoyant force equal to the weight of the displaced fluid. The measurement involved weighing the solid in air and subsequently in an auxiliary liquid of known density. Figure 9 illustrates the experimental setup used for density measurement through Archimedes' principle. The diagram shows the test rig where the sample is first weighed in air and then submerged in distilled water. By measuring the apparent weight loss when immersed, the system calculates the buoyant force, allowing for the determination of the sample's volume and, subsequently, its density and porosity. This setup provides a reliable, non-destructive method for assessing material quality in 3D-printed parts.

The density of the maraging steel can be determined as $\rho = \rho_{H2O}/[1 - (m_a/m)]$, where ρ_{H2O} represents the density of water, and m and m_a correspond to the true and apparent (immersed) masses, respectively. By applying this method, the density of the 3D-printed maraging steel was found to be 7,909 kg/m^3, which closely aligns with the reference density of 8,100 kg/m^3 for the conventionally manufactured material.[44] The experimental procedure utilized a weighing system with a 1-centigram resolution, yielding measured values of m = 121.41 and m_a = 106.06 g. With respect to the reference nominal density, a maximum porosity of around 2.34% can be inferred from the density testing.

3.4. Metallography and composition of the 3D-printed part

A qualitative experimental phase analysis was conducted using X-ray powder diffraction (XRD) with a conventional Bragg–Brentano diffractometer (D8 Advance DaVinci, Bruker AXS, Germany). The system utilized Ni-filtered Cu-Kα radiation (λ = 1.5406 Å), generated at 40 kV and 40 mA, and was equipped with a Lynxeye 1-D linear

detector. Data acquisition was performed over a 2θ range of 20–120°, with a step size of 0.02°, an exposure time of 0.5 s per step, and a spin rate of 15 rpm. Rietveld refinements were carried out using the TOPAS 5.0 software (Bruker AXS, Germany) following the fundamental parameters approach.

As illustrated in Figure 10, XRD analysis of the 3D-printed sample confirms a single-phase material with a BCC structure (space group Im-3m). The site occupancy parameters used in the Rietveld refinements align with the nominal elemental composition provided by the feedstock powder manufacturers (Table 1), indicating that Mo, Co, Ni, and Ti are in solid solution within the iron crystal lattice. The calculated lattice parameter was 0.28799661 nm, corresponding to a theoretical density of 8,216 kg/m^3. The estimated crystallite size was 26 nm, likely influenced by the rapid cooling rate characteristic of the AM process, which affects material fusion during 3D printing. Such a single-phase BCC structure is consistent with the low-carbon martensite typically formed in maraging steels under rapid solidification conditions, confirming that the LPBF process yields the expected martensitic matrix with minimal retained austenite. The slight Ni deficiency relative to the nominal composition might influence precipitation kinetics during the aging process. Nonetheless, our XRD and hardness measurements confirm that the material exhibits a stable martensitic structure typical of 1.2709 maraging steel, suggesting that this deviation did not meaningfully reduce the alloy's capacity to form the requisite intermetallic precipitates.

While the present microstructural investigation has primarily focused on surface and near-surface features using XRD and SEM, we acknowledge that a more in-depth analysis of the internal microstructure and detailed cross-sectional imaging could provide further insights into potential internal defects and grain orientation variations. Nonetheless, the current results robustly confirm that the printed maraging steel exhibits a uniform, fine-grained martensitic structure, thereby supporting the high quality of the fabricated parts.

The external top surface of the analyzed part, where roughness measurements were conducted, is shown in Figure 11. This SEM-acquired image reveals welding lines approximately 100 µm wide, along with a notable degree of material agglomeration, as indicated by the arrows. This agglomeration is likely a result of the combined effect of high laser intensity and the presence of small-diameter satellite particles. The chemical composition of the printed surface differs from that of the original powder particles, as detailed in Table 2. The most significant variation is an increase in Ti content and a corresponding decrease in Fe and Ni, suggesting Ti accumulation and the formation of Ni-Fe-Ti intermetallic compounds, which appear as black agglomerations in Figure 11. However, in areas of the printed surface where Fe-Ni-Ti particles are absent, the

Figure 9. Archimedes test rig for buoyancy and density measure

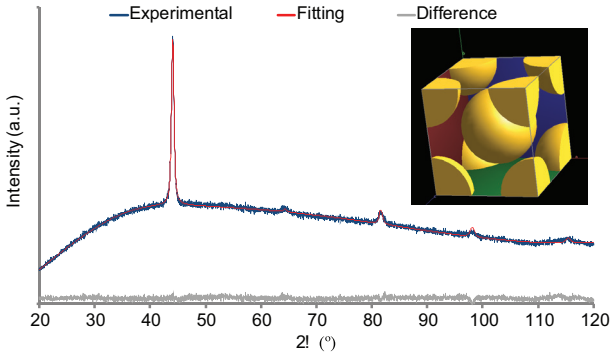

Figure 10. XRD diffraction pattern of 3D-printed material and representation of the corresponding BCC structure
Abbreviations: BCC: Body-centered cubic; XRD: X-ray powder diffraction

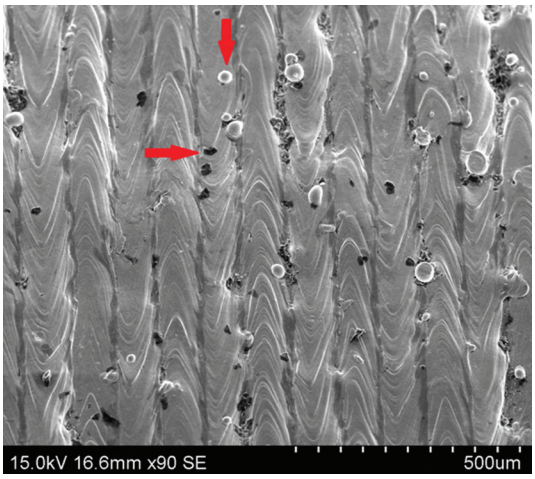

Figure 11. Scanning electron microscopy image of surface built part at 90× magnification

Table 2. Comparison of the measured chemical composition (wt.%) between the maraging steel powder and the fabricated Tool Steel 1.2709-A LMF (TRUMPF) part, including surface averages both with and without the presence of extraneous Ni-Fe-Ti intermetallic compounds

	Ni	Co	Mo	Ti	Fe
Powder	14.39	10.73	4.00	1.36	balance
Part surface (with IC)	12.81	7.40	3.38	8.87	balance
Part surface (without IC)	14.64	7.60	3.21	1.13	balance

chemical composition closely matches that of the original powder, as shown in Table 2.

3.5. Mechanical properties: Hardness (and strength)

The Rockwell hardness of a material was determined by applying a mild force followed by a major load. The zero position was established by the minor load. The primary load was imposed and subsequently withdrawn while the small load was maintained. The depth of penetration relative to the zero datum was determined using a dial, with a harder material yielding a lower reading. That is, the penetration depth is inversely related to the hardness. The primary advantage of Rockwell hardness is that it displays hardness values immediately, eliminating the need for laborious computations associated with other hardness measuring systems. It is frequently utilized in the fields of engineering and metallurgy. The commercial success of this method is attributed to its speed, dependability, durability, high resolution, and the ability to measure very small indentation areas. This is particularly advantageous for analyzing small samples, as in this study where we investigated the mechanical properties of a 3D-printed maraging steel demonstration part. The method allows for non-destructive testing, enabling direct inspection of local properties without damaging the part. Traditional methods, such as standard tensile testing, would require extracting material samples, which is not feasible for this application and investigation.

Of the various different Rockwell hardness scales, the "B" and "C" scales are the most often used. Both express hardness as a dimensionless arbitrary number. For the C scale used here, typically used in steel, hard cast irons, titanium, and other materials harder than 100 HRB, it uses a spheroconical diamond (Brale) indenter, made with a conical diamond of 120° angle and a tip radius of 0.2 mm (nominal dimensions), which is used for the hardest materials, with a preload of 10 kgf and major load of 150 kgf.

In this study, the hardness of the cut sample from the 3D-printed maraging steel part was evaluated on both the top and bottom surfaces using an EmcoTest DuraVision 20G5 hardness tester, equipped with an electronically controlled test cycle. To make the hardness (and non-destructive strength) assessment, 10 different hardness measurements were taken at random locations on both surfaces; for that purpose, the bottom surface, originally fused and cut from the substrate plate, was polished and the top surface was left as built. In addition, a heat treatment and age-hardening of 6 hours at 500°C was performed on a similar cut part, followed by another hardness measurement on the same surfaces.

Tensile strength and hardness are both indicative of a metal's resistance to plastic deformation and are therefore approximately proportional. In metal testing, indentation hardness exhibits a linear correlation with tensile strength, allowing for the non-destructive estimation of a material's tensile properties.[59] A straightforward conversion from Rockwell hardness (HRC) to Brinell hardness (HB) can be achieved using the recommended formulas derived elsewhere,[58] given by:

$$HB = 8.570 \cdot HRC + 27.6 \text{ (for } 31 < HRC < 40), \quad \text{(I)}$$

$$HB = 17.515 \cdot HRC - 401 \text{ (for } 51 < HRC < 60). \quad \text{(II)}$$

Similarly, according to the conversion tables provided by ASTM,[58] the corresponding converted Vickers hardness (HV) may be determined.

All the measured and converted hardness values obtained are presented in Table 3. As expected, the heat treatment results in higher hardness values due to the age-hardening process. The obtained HRC values fall within the expected and reported range: 33–37 HRC in the as-built and untreated state, and 50–54 HRC in the age-hardened state. For a confidence interval of 95%, the hardness deviation from the mean (error) is very small (<1%) for measurements performed on a prepared and polished surface in the non-heat-treated case. This indicates that the mechanical properties of the part are quite homogeneous and that measuring directly on the as-built surface increases the error to approximately <4%, leading to underestimated hardness (and strength) values. For the heat-treated case, the deviation in measurements on the polished surface is also small, but conversely, perhaps due to a reduction in ductility from the age-hardening and increased sensitivity of the results with pre-load of the indenter at the onset of the test, the unpolished surface results overestimate the true values. Nonetheless, the error with all methods remains small and acceptable, providing good mechanical properties estimation for engineering purposes.

From the determined values of the hardness employing the different values obtained for the different scales, both the yield (YS) and tensile strength (TS) can be estimated with different approaches, as presented in Table 4. The first approach considers the approximate interrelationships

Table 3. Hardness values obtained from testing the 3D-printed maraging steel demonstration part on the polished (bottom) and as-built unpolished (top) surfaces, along with hardness values converted to other scales

	Measurements at various point locations (HRC)	95% CI for the mean (HRC)	95% CI for the mean (HB)*	95% CI for the mean (HV)*
NHT and unpolished	35.45, 34.75, 38.90, 40.65, 33.58, 35.83, 35.33, 36.18, 40.08, 34.65	36.54±1.44 (±3.93%)	340.7±12.3 (±3.62%)	358.9±13.0 (±3.61%)
NHT and polished	38.83, 38.48, 39.75, 38.65, 39.50, 39.60, 39.15, 39.38, 39.08, 38.83	39.13±0.25 (±0.64%)	362.9±2.2 (±0.59%)	383.3±2.6 (±0.67%)
HT and unpolished	52.65, 51.20, 58.82, 51.63, 59.30, 53.82, 58.15, 55.42, 57.48, 56.40	55.49±1.77 (±3.19%)	570.9±31.0 (±5.43%)	605.1±33.1 (±5.46%)
HT and polished	52.63, 52.90, 53.53, 51.73, 53.58, 52.68, 53.42, 53.35, 52.35, 52.72	52.89±0.35 (±0.66%)	525.4±6.1 (±1.16%)	558.4±5.7 (±1.02%)

Note: *Converted values according to previous papers.[57,58]
Abbreviations: CI: Confidence interval; HT: Heat-treated; NHT: Non-heat-treated.

Table 4. 95% confidence interval for the mean yield and tensile strength values of the 3D-printed maraging steel demonstration part on the polished (bottom) and as-built unpolished (top) surfaces, estimated from the measured and converted hardness values

	From HRC values/MPa	From HB values/MPa	From HV values/MPa
NHT and unpolished	–	–	YS=941±37 (±3.96%)
	TS=1131±48 (±4.25%)	TS=1176±43 (±3.62%)	TS=1240±48 (±3.90%)
NHT and polished	–	–	YS=1011±7 (±0.73%)
	TS=1223±8 (±0.68%)	TS=1252±7 (±0.58%)	TS=1331±10 (±0.72%)
HT and unpolished	–	–	YS=1650±95 (±5.76%)
	TS=2128±135 (±6.35%)	TS=1969±107 (±5.43%)	TS=2160±123 (±5.72%)
HT and polished	–	–	YS=1515±16 (±1.09%)
	TS=1941±23 (±1.20%)	TS=1812±21 (±1.16%)	TS=1985±21 (±1.08%)

Notes: Estimates obtained using conversion tables and formulas derived from literature.[58,59]
Abbreviations: HT: Heat-treated; NHT: Non-heat-treated; TS: Tensile strength; YS: Yield strength.

between HRC hardness numbers and the estimated tensile strength of steels, as outlined in the conversion table provided by ASTM.[58] The second approach utilizes the HB values and the well-established rule of thumb for most steels, which states that the TS can be approximated by the equation TS = 3.45 · HB, with TS expressed in MPa. This empirical relationship, as noted previously,[59] indicates a linear variation of TS with HB, providing a convenient and practical method for the estimation of TS. Finally, the third approach uses the HV values and the correlation equations empirically established previously,[59] with the strength values in MPa given by:

$$YS = 2.876 \cdot HV - 90.7 \text{ and } TS = 3.734 \cdot HV - 99.8. \quad \text{(III)}$$

Consequently, the obtained hardness and TS values are consistent with those provided by the manufacturer and reported in the open literature, specifically: YS = 1000 ± 100 MPa and TS = 1100 ± 100 MPa, in the as-built and untreated state; YS = 1900 ± 100 MPa and TS = 1950 ± 100 MPa, in the age-hardened state. The results demonstrate that the hardness test can, in a straightforward and non-destructive way, be used to estimate the maraging steel TS; the YS is poorly estimated, however, since the empirical correlation established previously (Pavlina and Tyne[59]) was limited to YS up to 1700 MPa.

Although the values in Table 4 exhibit slight variations due to differences in the measurement methods, which are based on empirical rules, they remain within the expected range and align with the trends observed in the previously discussed hardness values. Both hardness and TS values align well with those reported by feedstock manufacturers and in the open literature,[36-38,47] namely: YS = 1000 ± 100 MPa and TS = 1100 ± 100 MPa, in the as-built and untreated state; YS = 1900 ± 100 MPa and TS = 1950 ± 100 MPa, in the age-hardened state. The results demonstrate that hardness testing can be a straightforward and non-destructive method to estimate the TS of maraging steel. However, the YS is poorly estimated since the empirical correlation established by Pavlina and Tyne[59] was limited to YS up to 1700 MPa, and maraging steels were not considered in the analysis.

4. Conclusion

This article presents an evaluation of the quality of 3D-printed maraging steel parts produced using LPBF

technology. It emphasizes crucial aspects such as powder uniformity, dimensional accuracy, surface roughness, and mechanical properties, all of which are vital for the successful application of AM in creating high-performance components.

Our investigation revealed that the demonstration 3D-printed parts exhibit exceptional dimensional quality, despite their complex geometries. Surface roughness measurements further demonstrated superior quality, with values well within the best-indicated standards for similar technologies. The theoretical calculations of material density using XRD and SEM corroborated the experimental results, indicating minimal porosity and defects in the material. While the material composition of the feedstock powder showed slight deviations from the nominal nickel values, these variations did not adversely affect mechanical performance. Notably, the maraging steel parts fabricated through LPBF displayed excellent mechanical properties, particularly in yield and tensile strength, aligning with both the manufacturer's specifications and values reported in existing literature. Non-destructive hardness measurements were found to be a reliable proxy for predicting tensile strength, reinforcing the potential of AM to produce robust mechanical parts.

Despite these positive findings, the study also highlights ongoing challenges related to feedstock quality and mechanical property predictability in printed parts. Variability in powder composition necessitates more rigorous quality control to ensure consistent performance. The current state of AM still grapples with uncertainties that need to be addressed to optimize metal component production fully. AM's ability to create intricate geometries while minimizing material waste underscores its superiority over traditional manufacturing methods. However, addressing the current scientific and technical challenges will require close collaboration between materials scientists, mechanical engineers, and quality assurance specialists. Nevertheless, this study adds to the expanding body of knowledge and reinforces the transformative potential of LPBF technology in producing vital mechanical components.

Acknowledgments

The collaboration of Pedro M. R. Resende from proMetheus/IPVC, Portugal, in the early phase of this work, is gratefully acknowledged by the authors.

Funding

The authors gratefully acknowledge: the support provided by the Foundation for Science and Technology (FCT) of Portugal, within the scope of the project of the "Research Unit on Materials, Energy, and Environment for Sustainability" (proMetheus), Ref. UID/05975/2020, financed by national funds through the FCT/MCTES; and the support provided within the scope of the "Agenda DRIVOLUTION: Transition to the Factory of the Future," project no. C632394276-0046698 with operation code 02/C05-i01.02/2022.PC644913740-00000022, within the framework of the Agendas/Mobilizing Alliances for Reindustrialization, Notice no. 2022-C05i0101-02, project 23, of the Recovery and Resilience Plan (PRR) of Portugal.

Conflicts of interest

The authors declare that they have no competing interests.

Authors' contributions

Conceptualization: César M. A. Vasques
Formal analysis: César M. A. Vasques
Funding acquisition: César M. A. Vasques, João C. C. Abrantes
Investigation: All authors
Methodology: All authors
Project administration: César M. A. Vasques
Writing – original draft: César M. A. Vasques
Writing – review & editing: All authors

Ethics approval and consent to participate

Not applicable.

Consent for publication

Not applicable.

Availability of data

Not applicable.

Further disclosure

This paper represents an extended and substantially developed version of the work initially presented in the conference paper titled "Vasques, C.M.A.; Resende, P.M.R.; Cavadas, A.M.S.; Abrantes, J.C.C., Quality Analysis of a Demonstration 3D-Printed Tool Steel Part, in Proceedings of the 2nd International Electronic Conference on Applied Sciences, 15–31 October 2021, MDPI: Basel, Switzerland (7 pages)." While the conference paper presented a preliminary subset of findings in the early phase of the investigations, the current paper offers significant advancements in both scope and content, incorporating new results, updated analyses, and deeper insights into the topic.

References

1. Thompson MK, Moroni G, Vaneker T, *et al.* Design for additive manufacturing: Trends, opportunities, considerations, and

constraints. *CIRP Ann*. 2016;65:737-760.

doi: 10.1016/j.cirp.2016.05.004

2. Attaran M. The rise of 3-D printing: The advantages of additive manufacturing over traditional manufacturing. *Bus Horiz*. 2017;60:677-688.

doi: 10.1016/j.bushor.2017.05.011

3. Grasso M, Colosimo BM. Process defects and *in situ* monitoring methods in metal powder bed fusion: A review. *Meas Sci Technol*. 2017;28:044005.

doi: 10.1088/1361-6501/aa5c4f

4. Lewandowski JJ, Seifi M. Metal additive manufacturing: A review of mechanical properties. *Ann Rev Mater Res*. 2016;46:151-186.

doi: 10.1146/annurev-matsci-070115-0320245

5. ASTM. *Additive Manufacturing-General Principles-Fundamentals and Vocabulary* (*ISO/ASTM 52900:2021*). United States: ASTM International; 2021.

doi: 10.1520/F3177-21

6. SLM Solutions Group AG. Available from: https://www.slm-solutions.com [Last accessed on 2021 Sep 16].

7. EOS GmbH-Electro Optical Systems. Available from: https://www.eos.info [Last accessed on 2021 Sep 16].

8. Concept Laser GmbH/GE Additive. Available from: https://www.ge.com/additive/who-we-are/concept-laser [Last accessed on 2021 Sep 16].

9. Trumpf GmbH & Co. KG. Available from: https://www.trumpf.com [Last accessed on 2021 Sep 16].

10. DM3D Technology, LLC. Available from: https://dm3dtech.com [Last accessed on 2021 Sep 16].

11. Optomec Inc. Available from: https://optomec.com [Last accessed on 2021 Sep 16].

12. Herzog D, Seyda V, Wycisk E, Emmelmann C. Additive manufacturing of metals. *Acta Mater*. 2016;117:371-392.

doi: 10.1016/j.actamat.2016.07.019

13. Chua C, Liu Y, Williams RJ, Chua CK, Sing SL. In-process and post-process strategies for part quality assessment in metal powder bed fusion: A review. *J Manuf Syst*. 2024;73:75-105.

doi: 10.1016/j.jmsy.2024.01.004

14. Thiede T, Mishurova T, Evsevleev S, Serrano-Munoz I, Gollwitzer C, Bruno G. 3D shape analysis of powder for laser beam melting by synchrotron X-ray CT. *Quantum Beam Sci*. 2019;3:3.

doi: 10.3390/qubs3010003

15. Zapico P, Giganto S, Barreiro J, Martínez-Pellitero S. Characterisation of 17-4PH metallic powder recycling to optimise the performance of the selective laser melting process. *J Mater Res Technol*. 2020;9:1273-1285.

doi: 10.1016/j.jmrt.2019.11.054

16. Aboulkhair NT, Simonelli M, Parry L, Ashcroft I, Tuck C, Hague R. 3D printing of aluminium alloys: Additive manufacturing of aluminium alloys using selective laser melting. *Prog Mater Sci*. 2019;106:100578.

doi: 10.1016/j.pmatsci.2019.100578

17. Sutton AT, Kriewall CS, Leu MC, Newkirk JW. Powder characterisation techniques and effects of powder characteristics on part properties in powder-bed fusion processes. *Virtual Phys Prototyp*. 2017;12:3-29.

doi: 10.1080/17452759.2016.1250605

18. Tian Y, Gora WS, Cabo AP, *et al*. Material interactions in laser polishing powder bed additive manufactured Ti6Al4V components. *Addit Manuf*. 2018;20:11-22.

doi: 10.1016/j.addma.2017.12.010

19. Zhang B, Li Y, Bai Q. Defect formation mechanisms in selective laser melting: A review. *Chin J Mech Eng*. 2017;30:515-527.

doi: 10.1007/s10033-017-0121-5

20. Malekipour E, El-Mounayri H. Common defects and contributing parameters in powder bed fusion AM process and their classification for online monitoring and control: A review. *Int J Adv Manuf Technol*. 2018;95:527-550.

doi: 10.1007/s00170-017-1172-6

21. Murr LE, Martinez E, Hernandez J, *et al*. Microstructures and properties of 17-4 PH stainless steel fabricated by selective laser melting. *J Mater Res Technol*. 2012;1:167-177.

doi: 10.1016/s2238-7854(12)70029-7

22. Facchini L, Vicente N Jr., Lonardelli I, Magalini E, Robotti P, Molinari A. Metastable austenite in 17-4 precipitation-hardening stainless steel produced by selective laser melting. *Adv Eng Mater*. 2010;12:184-188.

doi: 10.1002/adem.200900259

23. LeBrun T, Nakamoto T, Horikawa K, Kobayashi H. Effect of retained austenite on subsequent thermal processing and resultant mechanical properties of selective laser melted 17-4 PH stainless steel. *Mater Des*. 2015;81:44-53.

doi: 10.1016/j.matdes.2015.05.026

24. Kempen K, Yasa E, Thijs L, Kruth JP, Humbeeck JV. Microstructure and mechanical properties of selective laser melted 18Ni-300 steel. *Phys Procedia*. 2011;12:255-263.

doi: 10.1016/j.phpro.2011.03.033

25. Jägle EA, Choi PP, van Humbeeck J, Raabe D. Precipitation and austenite reversion behavior of a maraging steel produced by selective laser melting. *J Mater Res*. 2014;29:2072-2079.

doi: 10.1557/jmr.2014.204

26. Krakhmalev P, Yadroitsava I, Fredriksson G, Yadroitsev I. *In situ* heat treatment in selective laser melted martensitic AISI

420 stainless steels. *Mater Des*. 2015;87:380-385.

doi: 10.1016/j.matdes.2015.08.045

27. Niendorf T, Leuders S, Riemer A, Richard HA, Tröster T, Schwarze D. Highly anisotropic steel processed by selective laser melting. *Metall Mater Trans B*. 2013;44:794-796.

doi: 10.1007/s11663-013-9875-z

28. Zhao X, Song B, Zhang Y, Zhu X, Wei Q, Shi Y. Decarburization of stainless steel during selective laser melting and its influence on Young's modulus, hardness and tensile strength. *Mater Sci Eng A*. 2015;647:58-61.

doi: 10.1016/j.msea.2015.08.061

29. Song B, Zhao X, Li S, *et al*. Differences in microstructure and properties between selective laser melting and traditional manufacturing for fabrication of metal parts: A review. *Front Mech Eng*. 2015;10:111-125.

doi: 10.1007/s11465-015-0341-2

30. Majumdar JD, Pinkerton A, Liu Z, Manna I, Li L. Microstructure characterization and process optimization of laser assisted rapid fabrication of 316L stainless steel. *Appl Surf Sci*. 2005;247:320-327.

doi: 10.1016/j.apsusc.2005.01.039

31. Abd-Elghany K, Bourell D. Property evaluation of 304L stainless steel fabricated by selective laser melting. *Rapid Prototyp J*. 2012;18:420-428.

doi: 10.1108/13552541211250418

32. Carlton HD, Haboub A, Gallegos GF, Parkinson DY, MacDowell AA. Damage evolution and failure mechanisms in additively manufactured stainless steel. *Mater Sci Eng A*. 2016;651:406-414.

doi: 10.1016/j.msea.2015.10.073

33. Xu W, Brandt M, Sun S, *et al*. Additive manufacturing of strong and ductile Ti-6Al-4V by selective laser melting via *in situ* martensite decomposition. *Acta Mater*. 2015;85:74-84.

doi: 10.1016/j.actamat.2014.11.028

34. Thijs L, Sistiaga MLM, Wauthle R, Xie Q, Kruth JP, Humbeeck JV. Strong morphological and crystallographic texture and resulting yield strength anisotropy in selective laser melted tantalum. *Acta Mater*. 2013;61:4657-4668.

doi: 10.1016/j.actamat.2013.04.036

35. Carroll BE, Palmer TA, Beese AM. Anisotropic tensile behavior of Ti-6Al-4V components fabricated with directed energy deposition additive manufacturing. *Acta Mater*. 2015;87:309-320.

doi: 10.1016/j.actamat.2014.12.054

36. Wu W, Wang X, Wang Q, *et al*. Microstructure and mechanical properties of maraging 18Ni-300 steel obtained by powder bed based selective laser melting process. *Rapid Prototyp J*. 2020;26:1379-1387.

doi: 10.1108/rpj-08-2018-0189

37. Yao Y, Wang K, Wang X, *et al*. Microstructural heterogeneity and mechanical anisotropy of 18Ni-330 maraging steel fabricated by selective laser melting: The effect of build orientation and height. *J Mater Res*. 2020;35:2065-2076.

doi: 10.1557/jmr.2020.126

38. Mooney B, Kourousis K. A review of factors affecting the mechanical properties of maraging steel 300 fabricated via laser powder bed fusion. *Metals*. 2020;10:1273.

doi: 10.3390/met10091273

39. Takata N, Nishida R, Suzuki A, Kobashi M, Kato M. Crystallographic features of microstructure in maraging steel fabricated by selective laser melting. *Metals*. 2018;8:440.

doi: 10.3390/met8060440

40. Song J, Tang Q, Feng Q, *et al*. Effect of heat treatment on microstructure and mechanical behaviours of 18Ni-300 maraging steel manufactured by selective laser melting. *Opt Laser Technol*. 2019;120:105725.

doi: 10.1016/j.optlastec.2019.105725

41. Kürnsteiner P, Barriobero-Vila P, Bajaj P, *et al*. Designing an Fe-Ni-Ti maraging steel tailor-made for laser additive manufacturing. *Addit Manuf*. 2023;73:103647.

doi: 10.1016/j.addma.2023.103647

42. Su J, Li Q, Teng J, *et al*. Programmable mechanical properties of additively manufactured novel steel. *Int J Extrem Manuf*. 2024;7:015001.

doi: 10.1088/2631-7990/ad88bc

43. ASM International Handbook Committee. *Properties and Selection: Irons, Steels, and High-Performance Alloys*. Vol. 1. United States: ASM International; 1990.

doi: 10.31399/asm.hb.v01.9781627081610

44. Wikipedia. *Maraging Steel*. The Free Encyclopedia; 2021. Available from: https://en.wikipedia.org/w/index.php?title=maraging%20steel&oldid=1031815960 [Last accessed on 2021 Sep 16].

45. Hall A, Slunder C. *The Metallurgy, Behavior, and Application of the 18 Percent Nickel Maraging Steels. Report SP-5051*. National Aeronautics and Space Administration (NASA); 1968.

46. NiDI. *The 18 Percent Nickel Maraging Steels: Engineering Analysis. Publication No. 4419*. Canada: Nickel Development Institute (NiDI); 1976.

47. Protolabs. *Maraging Steel 1.2709*. Protolabs. Available from: https://www.protolabs.com/media/1022869/maraging-steel-1.pdf [Last accessed on 2025 Feb 26].

48. ASM International Handbook Committee. *Additive Manufacturing Processes*. Vol. 24. United States: ASM International; 2020.

doi: 10.31399/asm.hb.v24.9781627082907

49. Pannitz O, Sehrt JT. Transferability of process parameters in laser powder bed fusion processes for an energy and cost efficient manufacturing. *Sustainability*. 2020;12:1565.

doi: 10.3390/su12041565

50. Yun H, Dong L, Wang W, Bing Z, Xiangyun L. Study on the flowability of TC4 alloy powder for 3D printing. *IOP Conf Ser Mater Sci Eng*. 2018;439:042006.

doi: 10.1088/1757-899x/439/4/042006

51. Pagác M, Hajnys J, Petru J, Zlámal T. Comparison of hardness of surface 316L stainless steel made by additive technology and cold rolling. *Mater Sci Forum*. 2018;919:84-91.

doi: 10.4028/www.scientific.net/msf.919.84

52. Liverani E, Toschi S, Ceschini L, Fortunato A. Effect of selective laser melting (SLM) process parameters on microstructure and mechanical properties of 316L austenitic stainless steel. *J Mater Process Technol*. 2017;249:255-263.

doi: 10.1016/j.jmatprotec.2017.05.042

53. Strano G, Hao L, Everson RM, Evans KE. Surface roughness analysis, modelling and prediction in selective laser melting. *J Mater Process Technol*. 2013;213:589-597.

doi: 10.1016/j.jmatprotec.2012.11.011

54. Wang D, Liu Y, Yang Y, Xiao D. Theoretical and experimental study on surface roughness of 316L stainless steel metal parts obtained through selective laser melting. *Rapid Prototyp J*. 2016;22:706-716.

doi: 10.1108/RPJ-06-2015-0078

55. Leary M. Surface roughness optimisation for selective laser melting (SLM): Accommodating relevant and irrelevant surfaces. In: Brandt M editor. *Laser Additive Manufacturing: Materials, Design, Technologies, and Applications. Woodhead Publishing Series in Electronic and Optical Materials*. Ch. 4. United Kingdom: Woodhead Publishing; 2017. p. 99-118.

doi: 10.1016/B978-0-08-100433-3.00004-X

56. Vayssette B, Saintier N, Brugger C, Elmay M, Pessard E. Surface roughness of Ti-6Al-4V parts obtained by SLM and EBM: Effect on the high cycle fatigue life. *Procedia Eng*. 2018;213:89-97.

doi: 10.1016/j.proeng.2018.02.010

57. Iron-Foundry. *Rockwell Hardness* (*HRC, HRB*) *to Brinell Hardness* (*HB or BHN*) *Conversion*; 2024. Available from: https://www.iron-foundry.com/hardness-hrc-hrb-hb.html [Last accessed on 2024 Aug 05].

58. ASTM. *Standard Test Methods and Definitions for Mechanical Testing of Steel Products* (*ASTM A370-24*). United States: ASTM International; 2024.

doi: 10.1520/A0370-24

59. Pavlina E, Tyne CV. Correlation of yield strength and tensile strength with hardness for steels. *J Mater Eng Perform*. 2008;17:888-893.

doi: 10.1007/s11665-008-9225-5